

Tensional wrinkling of thin elastic sheets with two circular holes

Yang Liu^{a,b,c}, Sepideh Razavi^{d,e}, Pietro Cicuta^d, Dominic Vella^b, Alain Goriely^{b,*}

^a*Department of Mechanics, School of Mechanical Engineering, Tianjin University, Tianjin 300350, China*

^b*Mathematical Institute, University of Oxford, Oxford, OX2 6GG, UK*

^c*National Key Laboratory of Vehicle Power System, Tianjin 300350, China*

^d*Department of Physics, Cavendish Laboratory, University of Cambridge, Cambridge CB3 0HE, UK*

^e*School of Sustainable Chemical, Biological and Materials Engineering, University of Oklahoma, Oklahoma 73019, USA*

Abstract

A paradigm for the study of wrinkling in elastic sheet is the Lamé configuration, in which azimuthal wrinkles form in an annular sheet subjected to tensile loads at both edges. Since wrinkles are spatially extended, this instability provides a mechanism for stress transmission over long distances. A natural extension of this problem is wrinkling in sheets with multiple holes or broken symmetry. Here, we investigate tension-induced wrinkling in thin elastic sheets containing two circular holes by combining analytical modeling and experiments. The pre-buckled state is solved analytically using bipolar coordinates, enabling identification of the wrinkling threshold as a function of the distance between the two holes. Near-threshold wrinkling and interactions between wrinkles are analyzed, and we validate our theoretical predictions against experimental observations obtained through video imaging of spin-coated polystyrene sheets floating on liquid surfaces with controlled surface tension. Our results demonstrate that geometric symmetry breaking, such as the presence of a second hole, strongly influences wrinkle nucleation, orientation, and spatial extent. Beyond mechanics, these findings might provide a simple mechanism for cellular mechanosensing, where force transmission is amplified by mechanical instabilities.

Keywords: Ultrathin sheets, bipolar coordinates, elasticity, asymptotic analysis, capillary wrinkling

1. Introduction

Thin elastic sheets are much easier to bend than to stretch. Consequently, when subjected to compression (Bowden et al., 1998; Pocivavsek et al., 2008; Liu et al., 2025; Liu and Liu, 2026), poking (Vella et al., 2015; Dai and Lu, 2021; Wang et al., 2023), or being wrapped around a curved substrate (Hure et al., 2012; Hohlfeld and Davidovitch, 2015; Box et al., 2023), they tend to deform out of the substrate by forming wrinkles, thereby relieving compressive stresses. A particularly important and subtle class of instabilities is tension-induced wrinkling, in which a sheet subjected to stretching forces develops localized compressive stresses due to force balance and compatibility constraints (Cerdeja and Mahadevan, 2003; Wang et al., 2022; Chai et al., 2024). A paradigm for such class of problems is the classical Lamé problem, consisting of a thin elastic annulus subjected

*Corresponding author.

Email addresses: tracy_liu@tju.edu.cn (Yang Liu), srazavi@ou.edu (Sepideh Razavi), pc245@cam.ac.uk (Pietro Cicuta), dominic.vella@maths.ox.ac.uk (Dominic Vella), alain.goriely@maths.ox.ac.uk (Alain Goriely)

to different radial tensions applied at its inner and outer boundaries. The primary deformation can be solved exactly using linear elasticity theory (Timoshenko and Goodier, 1951). Whereas the radial principal stress is always tensile, the circumferential stress can become compressive, inducing wrinkling in a direction perpendicular to the compressive tractions (Coman and Haughton, 2006; Coman and Bassom, 2007). A ground-breaking experiment by Huang et al. (2007) demonstrated the formation of ordered wrinkles when a liquid droplet is deposited on a thin polystyrene (PS) film floating on water. This observation led to extensive research.

On the theoretical side, Vella et al. (2010) developed a physically based model and revealed that the presence of a liquid droplet generates azimuthal compression in the thin film, explaining the wrinkling reported in Huang et al. (2007). It also showed that the extent of the wrinkled region was underestimated. To resolve this discrepancy, tension-field theory was applied by Davidovitch et al. (2011), capturing the far-from-threshold wrinkling behavior. One of the most striking outcomes of such far-from-threshold analyses is the prediction that the spatial extent of wrinkles can be much larger than anticipated from near-threshold considerations. A refined analysis incorporating capillary-induced wrinkling was subsequently carried out by Schroll et al. (2013), successfully explaining the wrinkle length observed experimentally by Huang et al. (2007). Later, similar wrinkling phenomena were studied in annular geometries (Piñeirua et al., 2013; Paulsen et al., 2017), in dynamic settings (Box et al., 2019), as well as in the curved liquid sheets that encapsulate bubbles (Oratis et al., 2020; Davidovitch and Klein, 2024).

The study of wrinkling in thin films is not only motivated by the metrology of ultrathin films but also establishes connections with cellular mechanosensing and traction force microscopy for cells. In general, wrinkles effectively amplify weak compressive stresses, making them visible at macroscopic scales. From this perspective, wrinkling can be viewed as a mechanical analogue of signal propagation, in which information about force magnitude, direction, and geometry is encoded in the wrinkle morphology. In particular, along such wrinkles, cells can sense mechanical signals generated by other cells at a distance, which can regulate functions such as differentiation, proliferation, and apoptosis (Ladoux and Mège, 2017; Vining and Mooney, 2017; Van Helvert et al., 2018). Cultured cells typically contract to produce stresses in the compliant substrate beneath them, which can be large enough to trigger elastic instabilities such as wrinkling. For instance, cells cultured on thin elastic membranes have been observed to generate wrinkle patterns aligned with actin stress fibers, with wrinkle orientation reflecting the anisotropy of cellular forces (Style et al., 2014). Conversely, wrinkle characteristics can be used to estimate cellular traction (Li et al., 2022; Ardaševa et al., 2026). The study of Davidovitch et al. (2011) demonstrated that force signals can be transmitted over longer distances in wrinkled regions — this suggests that mechanical instabilities like wrinkling may also influence cellular sensing. However, research so far has focused on an idealized single cell, neglecting possible mechanical interactions between multiple cells. As a first step, it is natural to consider the case of two neighbouring cells, each generating a wrinkle field, but accounting for interactions. This motivates the present study, which considers a mechanical analog of this problem.

Beyond this specific problem, we point out that in many realistic systems, symmetry is typically broken by geometric defects, inclusions, or boundaries, all of which lead to highly anisotropic stress fields. Perforated sheets, in particular, provide a fertile platform for exploring how geometry controls wrinkling patterns. Paulsen et al. (2017) experimentally studied the wrinkle-to-fold transition in a floating annulus subjected to inner and outer tensions, establishing a geometric rule for mode transitions and highlighting the role of geometry in regulating thin-film patterns. Andrade-Silva and Adda-Bedia (2019) investigated a modified Lamé problem in which the circular hole is replaced by an elliptical one. It is worth mentioning that when geometric symmetry is fur-

ther broken, for example, by adding an additional hole, abundant (and complex) wrinkle patterns can emerge, as shown in preliminary experiments with a lattice of droplets deposited on a floating sheet (Huang, 2010). However, no theoretical model of this system has been presented so far. Since holes act as stress concentrators and introduce new length scales, the addition of another hole in the Lamé problem provides a rich system in which wrinkles may nucleate and interact in a manner distinct from the single-hole, axisymmetric case.

Here, we study tension-induced wrinkling in thin elastic sheets containing two circular holes — what we term the bipolar Lamé problem. To do so, we use analytical techniques to study the threshold and near-threshold behaviours as well as experiments to test these predictions and to start to indicate the behaviour far from threshold. More broadly, this study contributes to a growing perspective in solid mechanics that views wrinkling not merely as a failure mode or imperfection, but as a functional response that allows thin structures to adapt to complex loading and environmental conditions. Whether in engineered membranes, soft matter systems, or biological tissues, tension-induced wrinkling emerges as a powerful mechanism for stress redistribution and long-range mechanical communication. The remainder of the paper is organized as follows. In Section 2, we establish the mathematical formulation of the problem using bipolar coordinates. The exact solution for the pre-buckled state is derived in Section 3 using the technique of superposition. Section 4 focuses on the onset of wrinkling, including obtaining asymptotic formulae for the critical tension ratio at which wrinkling is first observed. The near threshold predictions for the spatial distribution of wrinkles are presented in Section 5, followed by the experimental investigation in Section 6. Finally, discussions and conclusions are provided in Section 7.

2. Problem formulation

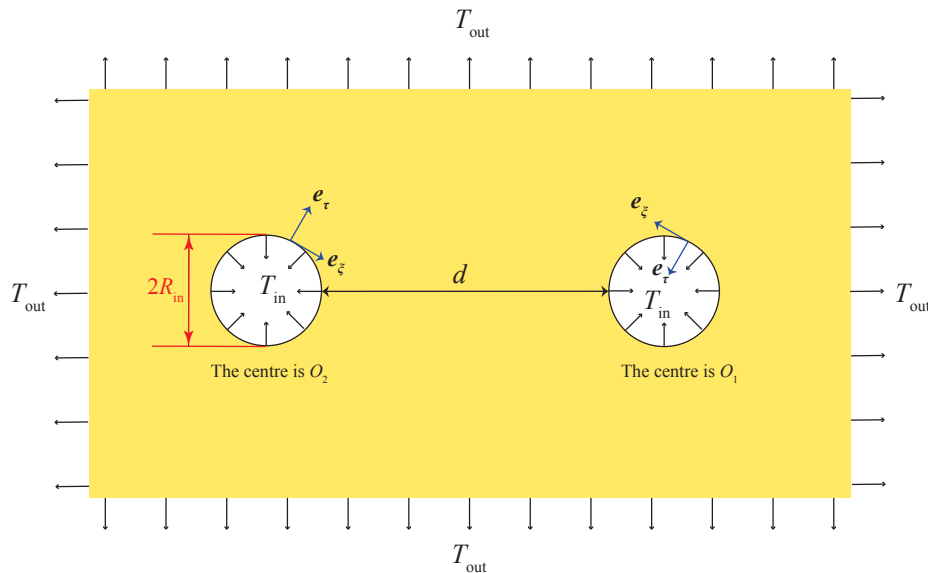


Figure 1: An infinite, elastic sheet (yellow) containing two equal circular holes of radius R_{in} and separated by a distance d is subjected to a tensional stress T_{in} at the internal surfaces and an all-around tension T_{out} at infinity.

We consider a thin, linearly-elastic membrane with two circular holes separated by a distance d . The holes have the same radius R_{in} and their centers are denoted O_1 and O_2 , respectively. The membrane is subject to a uniform normal tension T_{in} along the boundary of the holes as well as an isotropic tension T_{out} at infinity (Figure 1).

To describe the deformation, we use the bipolar coordinate system shown in Figure 2; here bipolar coordinates (τ, ξ) are assigned to a material point p whose Cartesian coordinates (x, y) satisfy:

$$x = \frac{a \sinh \tau}{\cosh \tau - \cos \xi}, \quad y = \frac{a \sin \xi}{\cosh \tau - \cos \xi}, \quad \tau \in \mathbb{R}, \quad \xi \in [0, 2\pi]. \quad (2.1)$$

Geometrically, $\xi = \angle po_1o_2$ while τ relates the relative distance to each of the hole centers, since

$$\tau = \ln \frac{r_2}{r_1}, \quad (2.2)$$

where r_i is the distance between p and O_i . Note that at infinity we have $\tau \rightarrow 0$ and $\xi \rightarrow 0$. In addition, we define two angular variables θ_1 and θ_2 , which will be employed in deriving asymptotic expressions.

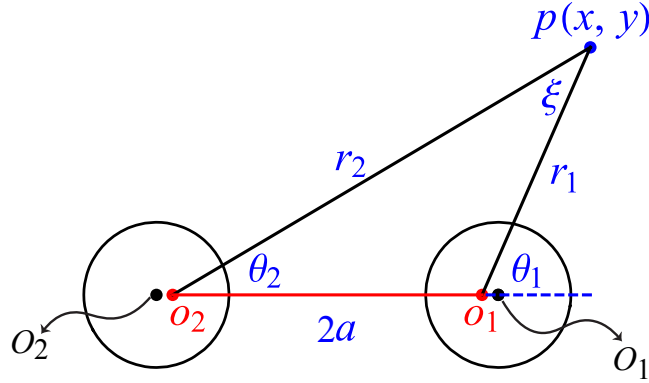


Figure 2: Definition of the bipolar coordinates (τ, ξ) . The two foci are located at $o_1 = (a, 0)$ and $o_2 = (-a, 0)$ (red points). The angle $\xi = \angle po_1o_2$, while $\tau = \ln(r_2/r_1)$ is a measure of the relative distance from the point $p(x, y)$ of interest. The two black circles represent the locations of the holes in our problem with the corresponding centers highlighted by black points, and denoted O_1 and O_2 , respectively.

We note that for constant ξ ,

$$x^2 + (y - a \cot \xi)^2 = \frac{a^2}{\sin^2 \xi}, \quad (2.3)$$

which is a circle with center $a \cot \xi$ and radius $a/|\sin \xi|$. Likewise, the contours of constant τ are characterized by

$$(x - a \coth \tau)^2 + y^2 = \frac{a^2}{\sinh^2 \tau}, \quad (2.4)$$

which are again circles.

In bipolar coordinates, the thin sheet with two circular holes shown in Figure 1 occupies the region

$$\Omega = \{-\tau_{\text{in}} \leq \tau \leq \tau_{\text{in}}, \quad 0 \leq \xi \leq 2\pi\}, \quad (2.5)$$

where τ_{in} is a positive constant related to the size of the circular hole(s). It then follows from (2.4)

that

$$R_{\text{in}} = \frac{a}{\sinh \tau_{\text{in}}}, \quad O_1 = (a \coth \tau_{\text{in}}, 0), \quad O_2 = (-a \coth \tau_{\text{in}}, 0). \quad (2.6)$$

In the above formulas we have used the Cartesian coordinates to determine the locations of O_1 and O_2 . Moreover, the closest distance between the two holes is

$$d = 2a \left(\coth \tau_{\text{in}} - \frac{1}{\sinh \tau_{\text{in}}} \right). \quad (2.7)$$

The scale factors for bipolar coordinates read

$$h_\tau = h_\xi \equiv h = \frac{a}{\cosh \tau - \cos \xi}. \quad (2.8)$$

Further details of the bipolar coordinate system are given in Appendix A. In this main text, we focus on the broader picture. In the absence of body force, the equilibrium equation for the Cauchy stress tensor $\boldsymbol{\sigma}$ is

$$\text{div } \boldsymbol{\sigma} = \mathbf{0}. \quad (2.9)$$

In addition, the compatibility equation for planar systems provides an extra condition:

$$\Delta (\text{tr } \boldsymbol{\sigma}) = 0, \quad (2.10)$$

where ‘ Δ ’ is the Laplacian operator and ‘tr’ the trace. The boundary conditions are

$$\begin{aligned} \sigma_{\tau\tau} &= T_{\text{in}}, \quad \sigma_{\tau\xi} = 0, \quad \text{at } \tau = \pm\tau_{\text{in}}, \\ \sigma_{\tau\tau} &= \sigma_{\xi\xi} = T_{\text{out}}, \quad \text{as } \tau \rightarrow 0, \quad \xi \rightarrow 0. \end{aligned} \quad (2.11)$$

3. Exact solution of the elasticity problem

In this section, we derive the exact solution to the elasticity problem described in Section 2. To this end, we introduce an Airy stress function $\psi(\tau, \xi)$ to ensure that the in-plane equilibrium equations (2.9) are satisfied automatically. The function ψ is determined by the compatibility equation (2.10), which becomes a bi-harmonic equation for ψ :

$$\Delta^2 \psi = 0, \quad (3.1)$$

or, explicitly:

$$\left(\frac{\partial^4}{\partial \tau^4} + 2 \frac{\partial^4}{\partial \tau^2 \partial \xi^2} + \frac{\partial^4}{\partial \xi^4} - 2 \frac{\partial^2}{\partial \tau^2} + 2 \frac{\partial^2}{\partial \xi^2} + 1 \right) \left(\frac{\psi}{h} \right) = 0. \quad (3.2)$$

First, we find a particular solution that satisfies the tension condition at infinity of the form (Ling, 1948):

$$\psi_0 = \frac{1}{2} T_{\text{out}} (x^2 + y^2) = \frac{a}{2} T_{\text{out}} h (\cosh \tau + \cos \xi), \quad (3.3)$$

where we have used (2.1) for the second equality. This stress function satisfies equation (3.2).

Specifically, it gives the following uniform stress field in the thin film

$$T_{\text{out}} (\mathbf{e}_\tau \otimes \mathbf{e}_\tau + \mathbf{e}_\xi \otimes \mathbf{e}_\xi). \quad (3.4)$$

Next, we consider the general solution of (3.2). Since both the geometry and the external loading are symmetric with respect to x (or equivalently ξ), we seek a separable solution ψ_1 of the form

$$\frac{\psi_1}{h} = \sum_{n=0}^{\infty} \phi_n(\tau) \cos n\xi. \quad (3.5)$$

Under this ansatz, equation (3.2) reduces to

$$\left(\frac{\partial^4}{\partial \tau^4} - 2(n^2 + 1) \frac{\partial^2}{\partial \tau^2} + (n^2 - 1)^2 \right) \phi_n(\tau) = 0. \quad (3.6)$$

The general solutions to (3.6) for $n \geq 2$ are given by

$$\phi_n(\tau) = a_n \cosh(n+1)\tau + b_n \sinh(n+1)\tau + c_n \cosh(n-1)\tau + d_n \sinh(n-1)\tau, \quad (3.7)$$

with a_n , b_n , c_n , and d_n being constants to be determined. For $n = 0$ and $n = 1$, the corresponding solutions take the form

$$\phi_0(\tau) = a_0 \cosh \tau + b_0 \sinh \tau + c_0 \tau \cosh \tau + d_0 \tau \sinh \tau, \quad (3.8)$$

$$\phi_1(\tau) = a_1 \cosh 2\tau + b_1 \sinh 2\tau + c_1 + d_1 \tau. \quad (3.9)$$

We further note that the problem is symmetric in τ , which requires that all coefficients b_i and d_i ($i = 1, 2, \dots$) vanish. Moreover, the mode ϕ_0 is discarded because it leads to multi-valued displacements (see Jeffery (1921) and Ling (1948)). Consequently, the eigenfunctions employed in the solution procedure can be expressed in the unified form

$$\phi_n(\tau) = a_n \cosh(n+1)\tau + c_n \cosh(n-1)\tau, \quad n \geq 1. \quad (3.10)$$

Based on the discussions in Jeffery (1921), we supplement (3.5) with an additional term to ensure that the solution is globally correct and that the boundary conditions can be satisfied:

$$K (\cosh \tau - \cos \xi) \log (\cosh \tau - \cos \xi), \quad (3.11)$$

where K is a constant. Then, the general solution takes the form

$$\begin{aligned} \frac{\psi}{h} &= \frac{\psi_0}{h} + \frac{\psi_1}{h} \\ &= \frac{a}{2} T_{\text{out}} (\cosh \tau + \cos \xi) + K (\cosh \tau - \cos \xi) \ln (\cosh \tau - \cos \xi) + \sum_{n=1}^{\infty} \phi_n(\tau) \cos n\xi. \end{aligned} \quad (3.12)$$

It follows from (A.7)–(A.9) that, once the condition $\psi_1(0, 0) = 0$ is imposed, all stress components derived from ψ_1 vanish at infinity. Hence, the stresses at infinity are solely due to the contribution

from ϕ_0 , ensuring that the uniform tension at infinity is preserved. This leads to the condition

$$\sum_{n=1}^{\infty} (a_n + c_n) = 0. \quad (3.13)$$

Substituting (3.12) into (A.7)-(A.9) yields

$$\begin{aligned} a\sigma_{\tau\tau} &= aT_{\text{out}} + \phi_1(\tau) - \frac{1}{2}K (\cosh 2\tau - 2 \cosh \tau \cos \xi + \cos 2\xi) \\ &+ \frac{1}{2} \sum_{n=1}^{\infty} \left((n-1)(n-2)\phi_{n-1}(\tau) - 2(n^2-1) \cosh \tau \phi_n(\tau) \right. \\ &\left. + (n+1)(n+2)\phi_{n+1}(\tau) - 2 \sinh \tau \phi'_n(\tau) \right) \cos n\xi, \end{aligned} \quad (3.14)$$

$$\begin{aligned} a\sigma_{\xi\xi} &= aT_{\text{out}} + \phi_1(\tau) - \frac{1}{2}\phi_1''(\tau) + \frac{1}{2}K (\cosh 2\tau - 2 \cosh \tau \cos \xi + \cos 2\xi) \\ &+ \frac{1}{2} \sum_{n=1}^{\infty} \left(2 \cosh \tau \phi_n''(\tau) - 2 \sinh \tau \phi'_n(\tau) + (n+2)\phi_{n+1}(\tau) - \phi_{n+1}''(\tau) - \phi_{n-1}''(\tau) \right. \\ &\left. - (n-2)\phi_{n-1}(\tau) \right) \cos n\xi, \end{aligned} \quad (3.15)$$

$$\begin{aligned} a\sigma_{\tau\xi} &= -K \sinh \tau \sin \xi + \frac{1}{2} \sum_{n=1}^{\infty} \left(2n \cosh \tau \phi'_n(\tau) - (n+1)\phi'_{n+1}(\tau) \right. \\ &\left. - (n-1)\phi'_{n-1}(\tau) \right) \sin n\xi, \end{aligned} \quad (3.16)$$

where primes here and hereafter signify differentiation with respect to the implied variable. For example, $\phi_1'(\tau) = d\phi_1/d\tau$.

Due to the symmetry of the problem with respect to τ and with the aid of (A.7) and (A.9), the boundary conditions (2.11)_{1,2} can be rewritten in the form

$$\begin{aligned} aT_{\text{out}} + \phi_1(\tau_{\text{in}}) - \frac{1}{2}K \cosh 2\tau_{\text{in}} + \frac{1}{2} \sum_{n=1}^{\infty} \left(2K\delta_{1n} \cosh \tau - K\delta_{2n} + (n-1)(n-2)\phi_{n-1}(\tau_{\text{in}}) \right. \\ \left. - 2(n^2-1) \cosh \tau \phi_n(\tau_{\text{in}}) + (n+1)(n+2)\phi_{n+1}(\tau_{\text{in}}) - 2 \sinh \tau_{\text{in}} \phi'_n(\tau_{\text{in}}) \right) \cos n\xi = aT_{\text{in}}, \end{aligned} \quad (3.17)$$

$$\frac{1}{2} \sum_{n=1}^{\infty} \left(2n \cosh \tau_{\text{in}} \phi'_n(\tau_{\text{in}}) - K\delta_{1n} \sinh \tau_{\text{in}} - (n+1)\phi'_{n+1}(\tau_{\text{in}}) - (n-1)\phi'_{n-1}(\tau_{\text{in}}) \right) \sin n\xi = 0. \quad (3.18)$$

These two equations give rise to two infinite sets of algebraic relations by requiring that the coefficients of $\cos n\xi$ ($n \geq 0$) and $\sin n\xi$ ($n \geq 1$) vanish independently. In particular, the constant term in (3.17) yields

$$aT_{\text{out}} - \frac{1}{2}K \cosh 2\tau_{\text{in}} + \phi_1(\tau_{\text{in}}) = aT_{\text{in}}, \quad (3.19)$$

while the coefficient of $\sin \xi$ in (3.18) reads

$$\cosh \tau_{\text{in}} \phi_1'(\tau_{\text{in}}) - \phi_2'(\tau_{\text{in}}) - K \sinh \tau_{\text{in}} = 0. \quad (3.20)$$

It is observed that equation (3.19) depends only on a_1 and c_1 through ϕ_1 . In contrast, equation (3.20) involves ϕ_2 . A careful inspection of (3.18) reveals that, by multiplying the coefficient of each $\sin n\xi$ term by $e^{-n\tau_{\text{in}}}$ and summing over all n , the contributions from ϕ_n with $n \geq 2$ can be eliminated. When combined with (3.19), this procedure yields a closed system of two equations for the unknowns a_1 and c_1 , namely

$$\begin{aligned} 2\phi_1(\tau_{\text{in}}) &= 2a(T_{\text{in}} - T_{\text{out}}) + K \cosh 2\tau_{\text{in}}, \\ \phi_1'(\tau_{\text{in}}) &= 2Ke^{-\tau_{\text{in}}} \sinh \tau_{\text{in}}. \end{aligned} \quad (3.21)$$

Moreover, by equating the coefficients of $\cos n\xi$ ($n \geq 1$) in (3.17) and $\sin n\xi$ ($n \geq 2$) in (3.18), we are able to derive the following recursion relations for $n \geq 2$ as follows

$$\begin{aligned} (n-1)n(n+1)\phi_n(\tau_{\text{in}}) \sinh \tau_{\text{in}} &= \phi_1'(\tau_{\text{in}}) (n \cosh n\tau_{\text{in}} - \coth \tau_{\text{in}} \sinh n\tau_{\text{in}}) \\ &\quad + K((n+1) \sinh(n-2)\tau_{\text{in}} - (n-1) \sinh n\tau_{\text{in}}), \\ n\phi_n'(\tau_{\text{in}}) \sinh \tau_{\text{in}} &= \phi_1'(\tau_{\text{in}}) \sinh n\tau_{\text{in}} - 2K \sinh(n-1)\tau_{\text{in}} \sinh \tau_{\text{in}}. \end{aligned} \quad (3.22)$$

(We note that these relations were already identified by Ling (1948), who considered the problem with no internal tension — i.e. $T_{\text{in}} = 0$ in our notation.) Making use of (3.21)₂, straightforward but technical manipulations of (3.22), together with standard identities for hyperbolic functions, yield for $n \geq 2$

$$\begin{aligned} \phi_n(\tau_{\text{in}}) &= -2e^{-n\tau_{\text{in}}} \frac{K(n \sinh \tau_{\text{in}} + \cosh \tau_{\text{in}})}{(n-1)n(n+1)}, \\ \phi_n'(\tau_{\text{in}}) &= 2e^{-n\tau_{\text{in}}} \frac{K \sinh \tau_{\text{in}}}{n}. \end{aligned} \quad (3.23)$$

We then substitute equation (3.10) into (3.21) and (3.23) to obtain

$$\begin{aligned} a_n &= \frac{2K(e^{-n\tau_{\text{in}}} \sinh n\tau_{\text{in}} + ne^{-\tau_{\text{in}}} \sinh \tau_{\text{in}})}{n(n+1)(\sinh 2n\tau_{\text{in}} + n \sinh 2\tau_{\text{in}})}, \quad n \geq 1 \\ c_n &= -\frac{2K(e^{-n\tau_{\text{in}}} \sinh n\tau_{\text{in}} + ne^{\tau_{\text{in}}} \sinh \tau_{\text{in}})}{n(n-1)(\sinh 2n\tau_{\text{in}} + n \sinh 2\tau_{\text{in}})}, \quad n \geq 2, \\ c_1 &= \frac{1}{2}(K \tanh \tau_{\text{in}} \cosh 2\tau_{\text{in}} + 2a(T_{\text{in}} - T_{\text{out}})). \end{aligned} \quad (3.24)$$

It follows from (3.13) that

$$K \left(\frac{1}{2} + \tanh \tau_{\text{in}} \sinh^2 \tau_{\text{in}} - 4 \sum_{n=2}^{\infty} M_n \right) = a(T_{\text{out}} - T_{\text{in}}), \quad (3.25)$$

where

$$M_n = \frac{e^{-n\tau_{\text{in}}} \sinh n\tau_{\text{in}} + n \sinh \tau_{\text{in}} (n \sinh \tau_{\text{in}} + \cosh \tau_{\text{in}})}{n(n^2 - 1)(\sinh 2n\tau_{\text{in}} + n \sinh 2\tau_{\text{in}})}. \quad (3.26)$$

In the case $T_{\text{in}} = 0$, equation (3.25) recovers the solution given by Ling (1948).

We next briefly show that the infinite series in (3.25) is convergent, so that it defines a well-

posed expression for K . For large n , we observe that

$$\sinh n\tau_{\text{in}} \sim \frac{1}{2}e^{n\tau_{\text{in}}}, \quad \sinh 2n\tau_{\text{in}} \sim \frac{1}{2}e^{2n\tau_{\text{in}}}. \quad (3.27)$$

It then follows that

$$M_n \sim 2 \sinh^2 \tau_{\text{in}} \frac{e^{-2n\tau_{\text{in}}}}{n}, \quad (3.28)$$

and hence

$$|M_n| \leq C_0 \frac{e^{-2n\tau_{\text{in}}}}{n}, \quad (3.29)$$

where C_0 is a positive constant depending only on τ_{in} . Clearly,

$$\sum_{n=2}^{\infty} \frac{e^{-2n\tau_{\text{in}}}}{n} \quad (3.30)$$

is convergent. Therefore, the series appearing in (3.25) converges for any given τ_{in} , ensuring that K is well defined.

We obtained an analytical solution given by (3.10) and (3.12) with all coefficients determined from (3.24) and (3.25). We observe from (3.25) that K is linear in a , and hence all coefficients in (3.24) are also linearly proportional to a . As a result, the stress components in (3.14)–(3.16) are independent of a . This is expected, since the two foci $(-a, 0)$ and $(a, 0)$ can be chosen arbitrarily and their positions should not affect the physical features of the problem. In the next section, we use this analytical solution to discuss possible wrinkling states.

4. Onset of wrinkling

Without loss of generality, in this section we use $a = 1$. To facilitate further analysis, we define the tension ratio

$$\gamma = \frac{T_{\text{in}}}{T_{\text{out}}}. \quad (4.1)$$

For the classic Lamé problem involving a single circular hole, it is well known that, in the thin sheet limit (when the bending stiffness tends to zero), the critical threshold for circumferential wrinkling is $\gamma = 2 := \gamma_{\text{cr}}$ (Coman and Haughton, 2006; Coman and Bassom, 2007; Davidovitch et al., 2011). We now solve the same problem for two holes, i.e. we determine the critical tension ratio as d/a varies, $\gamma_{\text{cr}}(d/a)$.

To measure the relative distance between holes, we introduce the parameter $\zeta = d/R_{\text{in}}$. Using (2.7), this parameter can be written as

$$\zeta = 2(\cosh \tau_{\text{in}} - 1). \quad (4.2)$$

Conversely, τ_{in} can be expressed in terms of ζ as

$$\tau_{\text{in}} = \text{arccosh} \left(\frac{\zeta}{2} + 1 \right). \quad (4.3)$$

We note that in the limit $\zeta \rightarrow \infty$ the two holes are far apart and the bipolar problem reduces to the classical Lamé problem. We therefore anticipate that $\gamma_{\text{cr}}(\zeta) \rightarrow 2$ as $\zeta \rightarrow \infty$.

To determine the value of $\gamma_{\text{cr}}(\zeta)$, we note that thin sheets with negligible bending stiffness have negligible resistance to compression. As a result, the onset of wrinkling can be identified by finding when compressive stresses first arise. To this end, we determine the lower principal stress σ_2 as

$$\sigma_2(\tau, \xi) = \frac{\sigma_{\tau\tau} + \sigma_{\xi\xi}}{2} - \sqrt{\left(\frac{\sigma_{\tau\tau} - \sigma_{\xi\xi}}{2}\right)^2 + \sigma_{\tau\xi}^2}. \quad (4.4)$$

Figure 3 illustrates the spatial distribution of the normalized stress component σ_2/T_{out} for a tension ratio $\gamma = 3$ and an inner traction $\tau_{\text{in}} = 2$. The two circular holes are represented by the white disks, while the black curves indicate contours of constant stress. For this configuration, the radius of each circular hole is $R_{\text{in}} = 1/\sinh 2 \approx 0.275721$, and the distance between the two holes is $d \approx 1.52319$ (see (2.7)). It is evident from the figure that regions of compressive stress develop in the vicinity of both holes. Moreover, the contours corresponding to a given stress level exhibit shapes resembling Cassini ovals. We emphasize that the analytical solution in the previous section is valid only for the primary deformation, for which no instability is present — since very thin sheets cannot support compression, the compressive stress observed in figure 3 would not be observed experimentally.

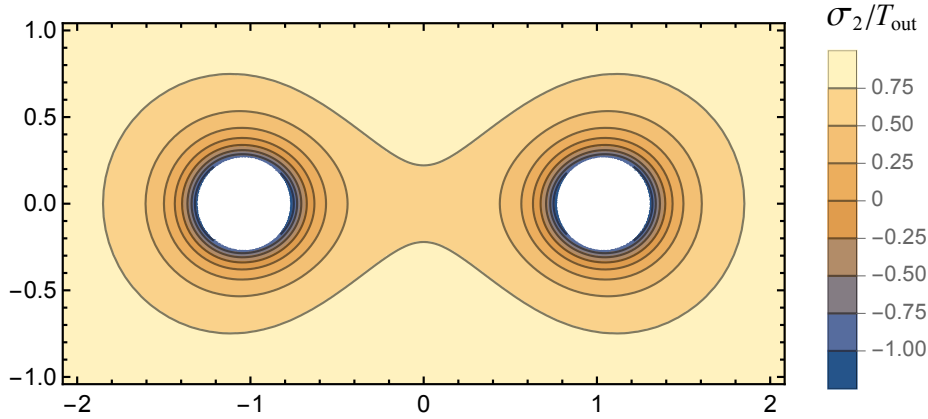


Figure 3: The distribution of the normalized principal stress σ_2/T_{out} for $\tau_{\text{in}} = 2$ and $\gamma = 3$.

To identify where the minimum value of σ_2 occurs in the sheet, we plot in Figure 4 the normalized stress as either τ or ξ varies. From the left panel, we observe that σ_2 attains its global minimum at $\xi = \pi$. By contrast, the right panel shows that σ_2 reaches its minimum at $\tau = \tau_{\text{in}}$. Accordingly, the lowest stress in the sheet is attained at $(\tau, \xi) = (\tau_{\text{in}}, \pi)$, and the critical tension ratio γ_{cr} for the onset of wrinkling can be identified from the condition

$$\sigma_2(\tau_{\text{in}}, \pi, \gamma_{\text{cr}}) = 0. \quad (4.5)$$

Substituting (4.3) into the critical condition (4.5) yields an expression for the critical tension ratio γ_{cr} for a given ζ . The resulting behaviour of $\gamma_{\text{cr}}(\zeta)$ and a phase diagram are shown in Figure 5; this illustrates the regions in parameter space associated with wrinkled or flat sheets. The blue curve gives the threshold γ_{cr} . As γ increases from one, for a given ζ , wrinkling appears for $\gamma > \gamma_{\text{cr}}$. The function $\gamma_{\text{cr}}(\zeta)$ is a monotonically increasing function that tends asymptotically to $\gamma = 2$ as $\zeta \rightarrow \infty$. We note also that the limit $\zeta \rightarrow 0$, corresponds to the limit in which the two

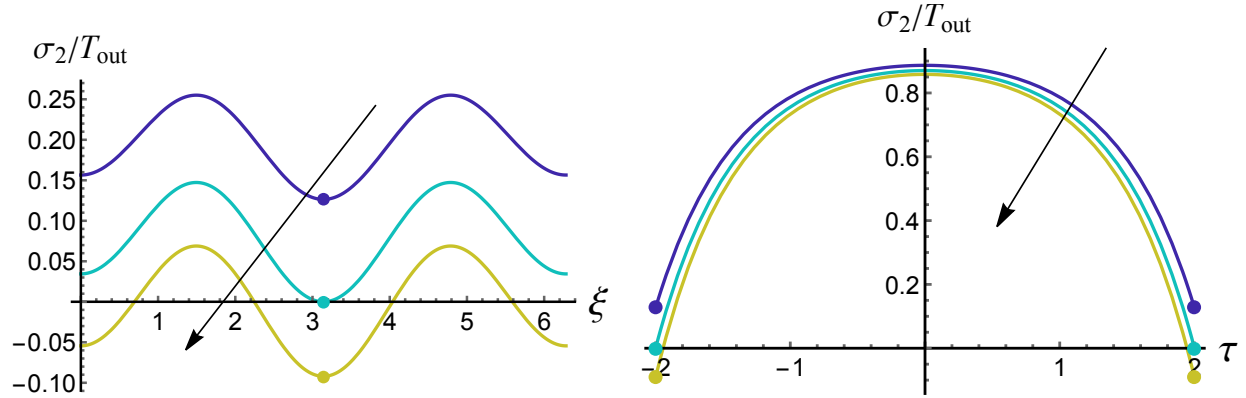


Figure 4: Dependence of the normalized stress σ_2/T_{out} on ξ (left panel) and τ (right panel) for $\tau_{\text{in}} = 2$ and $\gamma \in \{1.8, \gamma_{\text{cr}} = 1.9158, 2\}$. The arrows in each figure indicate the direction of increasing γ . In the left panel, $\tau = 2$, while in the right panel $\xi = \pi$. The global minimum is highlighted with points in each panel.

circular holes just touch. In this case, the critical tension ratio approaches 1. We discuss this limit in more detail later, but for now note that, in comparison with the single-hole case, the presence of an additional hole always promotes an earlier onset of instability. A similar early wrinkling phenomenon was reported by Andrade-Silva and Adda-Bedia (2019) when the circular hole in the classical Lamé problem is replaced by an elliptical hole. We now turn to determining asymptotic relationships for γ_{cr} that are valid when ζ is large or small.

4.1. Large hole separations: $\zeta \gg 1$

In the large separation limit, we consider an asymptotic expansion in $1/\zeta$:

$$\frac{\sigma_2(\zeta, \pi, \gamma)}{T_{\text{out}}} = 2 - \gamma + \frac{4 - 4\gamma}{\zeta^2} + \frac{8\gamma - 8}{\zeta^3} + \frac{8 - 8\gamma}{\zeta^4} + \mathcal{O}(\zeta^{-5}). \quad (4.6)$$

Substituting this expansion into (4.5), we obtain a four-term asymptotic approximation for the critical tension ratio,

$$\gamma_{\text{cr}} = 2 - \frac{4}{\zeta^2} + \frac{8}{\zeta^3} + \frac{8}{\zeta^4} + \mathcal{O}(\zeta^{-5}). \quad (4.7)$$

Based on this result, we further apply the Padé approximant to obtain a rational function (Baker and Graves-Morris, 1996)

$$\gamma_{\text{cr}} \approx \frac{2\zeta^2 + 4\zeta + 8}{\zeta^2 + 2\zeta + 6}. \quad (4.8)$$

The expansion of (4.8) in powers of $1/\zeta$ coincides with (4.7) up to the truncated order, while providing a substantially improved approximation and thereby extending the effective range of validity of the asymptotic analysis.

The two approximate solutions valid when $\zeta \gg 1$, i.e. (4.7) and (4.8), are compared with the (numerically-determined) exact solution in Figure 6. It is observed that the four-term asymptotic solution (4.7) (red dotted curve) remains accurate up to $\zeta \sim 6$, which is remarkable given that the underlying assumption of the asymptotic analysis is $\zeta \gg 1$. More importantly, the Padé approximant (4.8) (red dashed curve) exhibits excellent agreement with the exact solution even

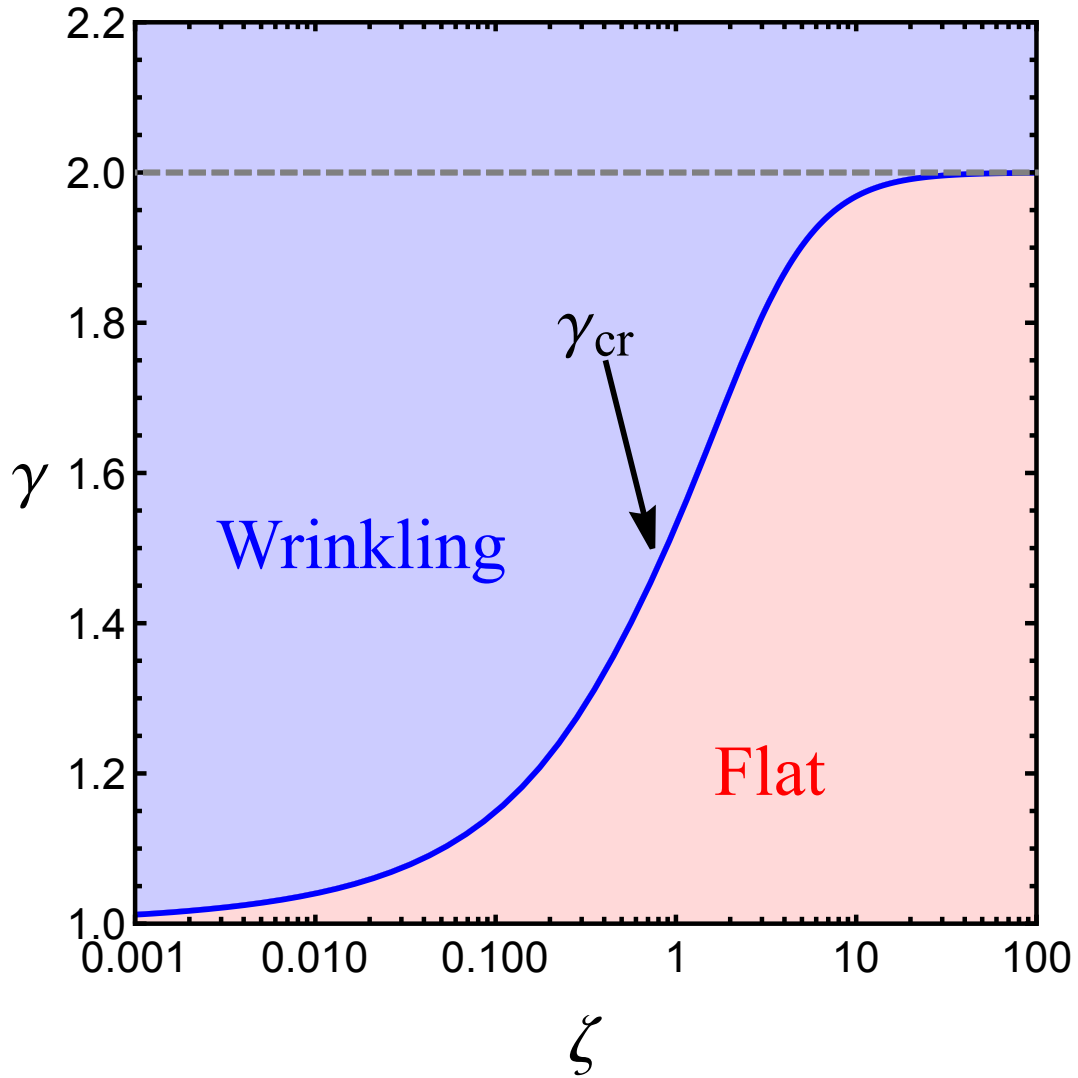


Figure 5: Phase diagram showing the transition between wrinkled and flat configurations in the γ - ζ plane. The blue solid line denotes the critical tension ratio γ_{cr} , while the gray dashed line (corresponding to $\gamma = 2$) indicates the critical tension ratio for the Lamé problem.

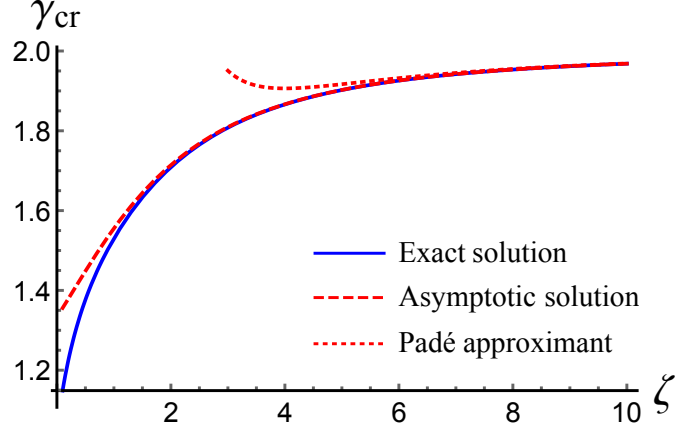


Figure 6: Comparisons between the exact solution (blue solid curve) and the asymptotic solutions for $\zeta \gg 1$. The predictions (4.7) (dotted) and (4.8) (dashed) recover the numerically-determined exact behaviour with the latter being essentially exact for $\zeta > 2$.

down to $\zeta \sim 1.5$. This demonstrates that the Padé approximant provides a significantly improved approximation and can be reliably used to predict the wrinkling threshold over a much wider range of ζ .

4.2. Small hole separations: $\zeta \ll 1$

From Figure 5, we also observe that $\gamma_{cr} \rightarrow 1$ as $\zeta \rightarrow 0$. This implies that when the two holes are sufficiently close, wrinkling occurs as soon as T_{in} slightly exceeds T_{out} . In this limit, it can be shown that $\sum_{n=2}^{\infty} M_n$ takes the limit (Ling, 1948)

$$\sum_{n=2}^{\infty} M_n = \sum_{n=2}^{\infty} \frac{1}{n(n^2 - 1)} - 2\tau_{in}^2 \int_0^{\infty} \frac{\sinh^2 \zeta - \zeta^2}{\zeta^3(\sinh 2\zeta + 2\zeta)} d\zeta. \quad (4.9)$$

In view of this, we deduce that K is well defined as $\zeta \rightarrow 0$ (or equivalently $\tau_{in} \rightarrow 0$). However, it is known that the stresses when expressed as an infinite series (3.14)-(3.16), do not converge uniformly when $\zeta \rightarrow 0$ (Callias and Markenscoff, 1989; Zimmerman, 1988). Consequently, the limit operator and the summation operator cannot be interchanged, and we are therefore unable to derive a valid asymptotic solution for the critical tension ratio γ_{cr} . Nevertheless, Figure 5 suggests that the asymptotic behaviors in the limits $\zeta \rightarrow 0$ and $1/\zeta \rightarrow 0$ are qualitatively similar. In addition, as detailed in Zimmerman (1988); Callias and Markenscoff (1993); Wu and Markenscoff (1996), the maximum stress in this case blows up in the order of $\zeta^{1/2}$ if T_{in} vanishes. Motivated by this and the ansatz in (4.7), we fit the exact solution using a series expansion in powers of $\zeta^{1/2}$. Retaining only two significant figures in the fitted coefficients, we obtain

$$\gamma_{cr} \approx 1 + \frac{2}{5}\zeta^{1/2} + \frac{27}{100}\zeta - \frac{7}{50}\zeta^{3/2}. \quad (4.10)$$

A comparison between the fitted formula (4.10) and the exact solution is presented in Figure 7. It can be seen that the fitting expression (4.10) provides good agreement with the exact solution even for values of ζ as large as 2.5.

Combining (4.8) and (4.10), we provide a complete set of explicit solutions for the wrinkling initiation over the entire range of ζ , which is useful for accurately predicting the onset of wrinkling.

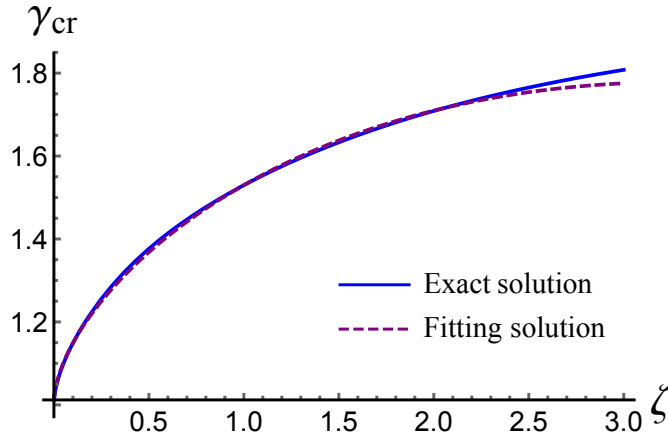


Figure 7: Comparison between the exact (but numerically-determined) prediction for the critical tension ratio at buckling, γ_{cr} , (solid blue curve) and the fit (4.10) (dashed purple curve) as the distance, ζ , between the two holes is varied.

5. Extent of wrinkles

5.1. Near-threshold wrinkling

As γ exceeds γ_{cr} , wrinkles are induced to release compressive stresses in the sheet. Consequently, the stresses must be updated to account for this change. In general, tension-field theory can be used to approximate the stress distribution by enforcing $\sigma_2 = 0$ in regions where compressive stress would otherwise occur (Mansfield, 1969; Pipkin, 1986; Steigmann and Pipkin, 1989a,b; Steigmann, 1990). In this framework, the whole sheet is divided into two regions connected through an interface: an inner wrinkled region where $\sigma_2 = 0$, and an outer flat tensile region. For the Lamé problem, Davidovitch et al. (2011) applied tension-field theory to obtain the wrinkled region. In particular, they showed that the maximum stress decays in inverse proportion to the distance from the hole center. When compared to the faster (inverse square) decay that occurs in the purely tensile case, we see that wrinkling allows the stress signal to spread over longer distances. In particular, while the size of the region in which compression is observed would grow like $\sqrt{\gamma - \gamma_{cr}}$ if compressive stress were resisted, wrinkling (and the associated relaxation of compression) means that the size of the wrinkled region grows linearly with $\gamma > \gamma_{cr}$.

Although tension-field theory is a powerful tool for determining the actual extent of wrinkling, its direct application to the present problem is not straightforward because of the loss of geometric symmetry. In particular, the approach employed by Davidovitch et al. (2011) cannot readily be extended to this setting. Nevertheless, when the tension ratio γ is only slightly above the critical value γ_{cr} , that is, in the near-threshold regime, we expect that the wrinkled region may still be described using the purely tensile elastic solution presented in Section 3 (Davidovitch et al., 2011). Motivated by this observation, we focus in this subsection on analyzing the wrinkled region in the near-threshold case, with the aim of providing new insight into where wrinkles first emerge in an elastic sheet containing two circular holes.

5.1.1. Numerical results for intermediate hole separations, $\zeta = \mathcal{O}(1)$

When the two holes are far apart, the system behaves like the classical Lamé problem. For this reason, we first focus on configurations in which the two holes are relatively close. To examine the near-threshold regime, the tension ratio is prescribed as $\gamma = 1.1\gamma_{cr}$ or $\gamma = 1.3\gamma_{cr}$, allowing us to qualitatively trace the evolution of the wrinkled region. The boundary of the wrinkled area is

identified by locating the zero contour of the lower principal stress σ_2 for a given $\gamma > \gamma_{\text{cr}}$. The resulting wrinkled regions are shown in blue in Figure 8. We consider three representative values of the hole separation parameter, namely $\zeta = 0.1, 1$, and 3.

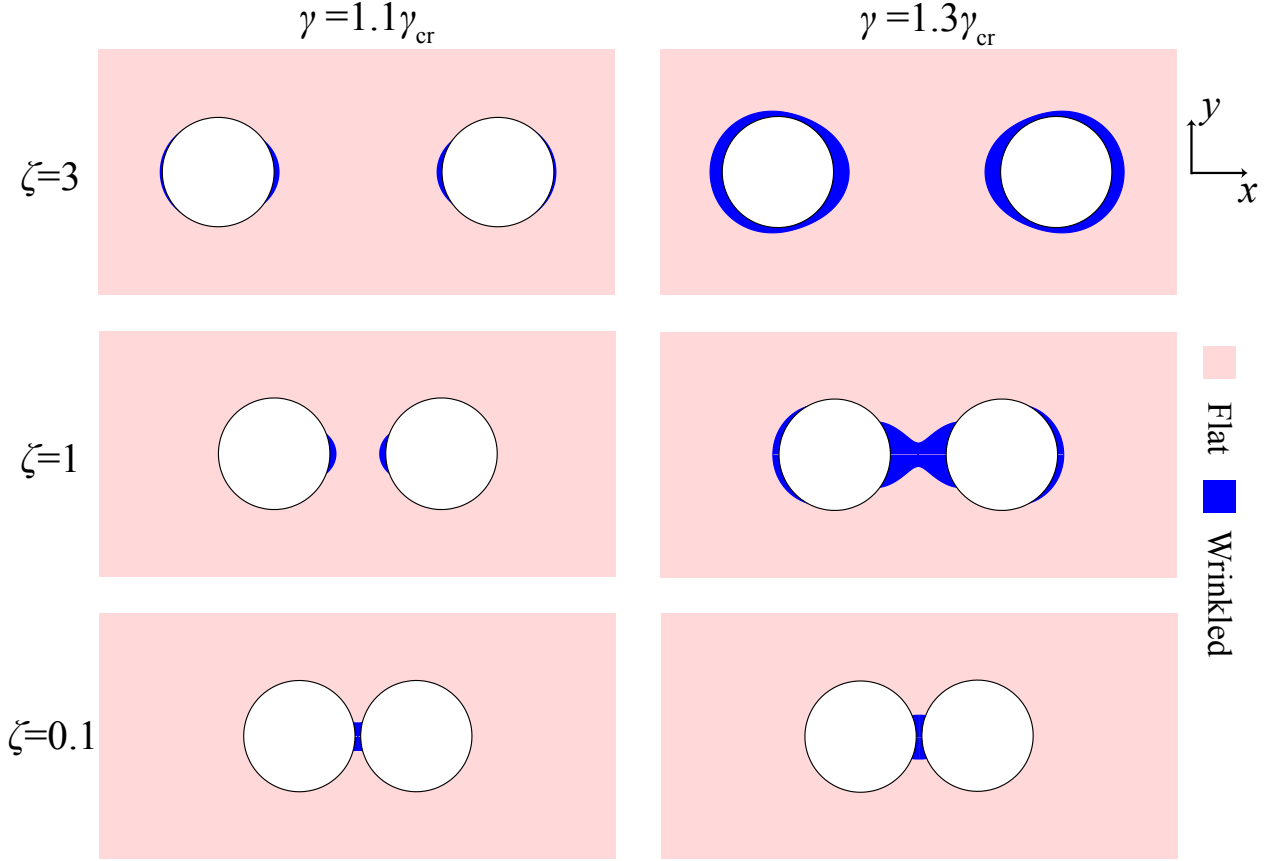


Figure 8: Representation of the wrinkled regions (highlighted in blue) for γ close to γ_{cr} and different values of the scaled hole separation $\zeta = d/R_{\text{in}}$.

For $\zeta = 3$ and $\gamma \gtrsim \gamma_{\text{cr}}$, wrinkles start at the front and rear of each hole. Recall that wrinkle initiation occurs at (τ_{in}, π) , corresponding to the Cartesian locations $(-d/2, 0)$ and $(d/2, 0)$, where d denotes the distance between the two holes. Consequently, wrinkles first develop in the forward and backward directions along the x -axis. As γ increases to $1.3\gamma_{\text{cr}}$, wrinkles are mainly concentrated on both lateral sides of the holes. This suggests that when γ is sufficiently large, the wrinkled regions surrounding the two holes will eventually merge at the center of the sheet. When the holes are closer ($\zeta = 1$), wrinkles initially appear only on the facing sides of the holes. With further increases in γ , wrinkles extend into the region between the two holes merging together, while additional wrinkling also develops on the outer sides. This behavior is consistent with the experimental observations reported in Figure 4.4(B) of Huang (2010). Although the overall wrinkled extent is significantly amplified due to stress redistribution in the sheet, the present near-threshold analysis is still able to capture the primary geometric features of the wrinkled patterns. Finally, we consider the extreme case $\zeta = 0.1$, where the two holes are very close. In this regime, wrinkles are confined to the region between the holes and gradually expand in the y -direction as γ increases from $1.1\gamma_{\text{cr}}$ to $1.3\gamma_{\text{cr}}$.

5.1.2. Widely separated holes: $\zeta \gg 1$

Turning now to the case $\zeta \gg 1$ where the two holes are far apart we recall that we were previously able to obtain an asymptotic solution, (4.7), for the critical tension ratio. In the same way, we can carry out an asymptotic analysis to derive explicit formulae for the stress components when $\zeta \gg 1$. Details are provided in Appendix B. In summary, we are able to express the principal stress σ_2 in (4.4) as a series of ζ (using (B.5)). An approximation for the boundary of the wrinkled area may then be determined from the condition $\sigma_2 = 0$. We find that the boundary of the wrinkled region is given by $r_1 = W_{\text{NT}}(\theta_1)$ where

$$W_{\text{NT}}(\theta_1) = (\gamma-1)^{1/2}R_{\text{in}} + \frac{R_{\text{in}} \cos \theta_1}{\zeta} + \frac{1}{4\zeta^2} \left(\frac{(2\gamma^2 - 4\gamma + 9) \cos 2\theta_1}{\sqrt{\gamma-1}} - 8 \cos \theta_1 \right) R_{\text{in}} + \mathcal{O}(\zeta^{-3}), \quad (5.1)$$

with θ_1 as defined in Figure 2. It is found that (5.1) reduces to the $(\gamma-1)^{1/2}R_{\text{in}}$ as $\zeta \rightarrow \infty$, which is identical to the result for the Lamé problem (Davidovitch et al., 2011).

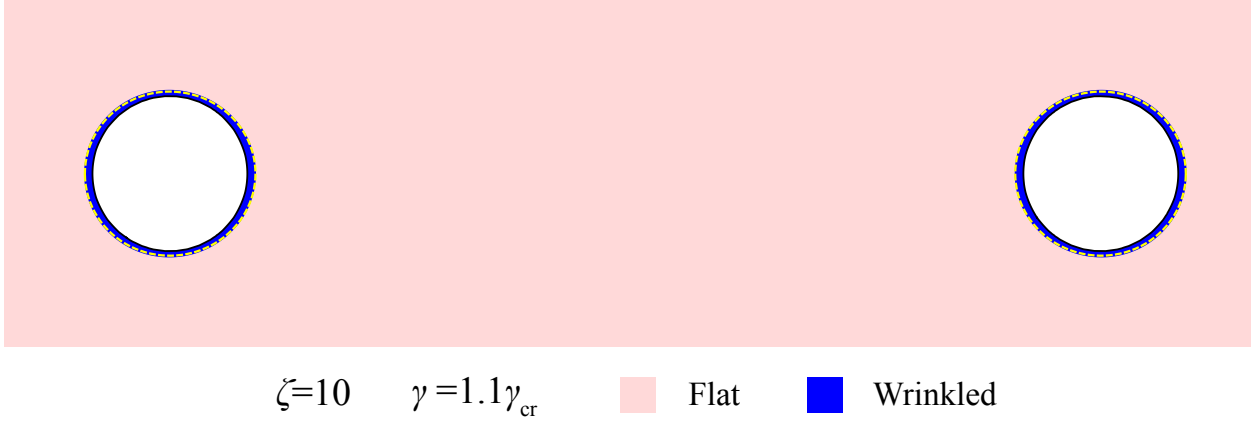


Figure 9: The extent of wrinkles in the near-threshold regime when the two holes are far apart. The dashed curve indicates the approximate boundary of wrinkled region predicted by (5.1), which coincides well with the extent of the region in which compression exists (shaded blue).

The example, shown in Figure 9 demonstrates excellent agreement between the two solutions. When the two holes are well separated, they do not interact with each other and the wrinkling behavior is locally that of the classical Lamé problem: wrinkles develop more or less uniformly around the periphery of the hole.

5.2. Far-from-threshold wrinkling when the two holes are far apart

The stress distribution shown in Figure 3 is replaced by an energetically favorable wrinkled state when $\gamma > \gamma_{\text{cr}}$. The main idea when applying the tension-field theory to the Lamé problem is to set the compressive stress to zero and then solve the modified equilibrium equations (Pipkin, 1986; Steigmann, 1990; Davidovitch et al., 2011). Making use of (4.4), we find that, in the wrinkled region,

$$\sigma_2 = 0 \implies \sigma_{\tau\xi}^2 - \sigma_{\tau\tau}\sigma_{\xi\xi} = 0 \iff \det \boldsymbol{\sigma} = 0. \quad (5.2)$$

We note that the final relation is applicable in any coordinate system.

In contrast to the Lamé problem, the τ - and ξ -axes no longer coincide with the principal directions. Consequently, equations (2.9) and (5.2) must be solved simultaneously. Moreover,

the profile of the boundary separating the wrinkled and flat regions is typically unknown, which makes the application of tension-field theory challenging in general. Nevertheless, in the far limit of well-separated holes, $\zeta \rightarrow \infty$, we can perform a perturbation analysis based on the exact far-from-threshold solutions (Davidovitch et al., 2011).

To do so, we take $1/\zeta$ as a small parameter and use it to construct an asymptotic solution. Without loss of generality, we fix the right hole, and move the left hole away in Figure 2, which is equivalent to restricting attention to the right half-plane. In doing so, we select a polar coordinate system centered at the right focus. Accordingly, the coordinate r measures the distance from any material point to this new origin, while θ denotes the usual polar angle. We further assume that when γ is much larger than the critical value γ_{cr} , the wrinkled region is confined to $r \leq W_{\text{FT}}(\theta)$ where

$$W_{\text{FT}}(\theta) = R_{\text{in}} \frac{\gamma}{2} + \frac{W^{(1)}(\theta)}{\zeta} + \mathcal{O}(\zeta^{-2}). \quad (5.3)$$

Here, the leading-order term is the far-from-threshold solution of the Lamé problem (Davidovitch et al., 2011), which is axisymmetric. $W^{(1)}(\theta)$ (and all quantities with superscript (1)) is then an unknown function, to be determined in the subsequent analysis, that captures the leading-order deviations from axisymmetry.

In the wrinkled region, we seek a perturbative solution of the form

$$\sigma_{rr}^{\text{in}} = T_{\text{in}} \frac{R_{\text{in}}}{r} + \frac{\sigma_{rr}^{(1)}(r, \theta)}{\zeta} + \mathcal{O}(\zeta^{-2}), \quad \sigma_{r\theta}^{\text{in}} = \frac{\sigma_{r\theta}^{(1)}(r, \theta)}{\zeta} + \mathcal{O}(\zeta^{-2}), \quad \sigma_{\theta\theta}^{\text{in}} = \frac{\sigma_{\theta\theta}^{(1)}(r, \theta)}{\zeta^2} + \mathcal{O}(\zeta^{-3}), \quad (5.4)$$

where the leading-order (and axisymmetric) solution is given in Davidovitch et al. (2011), and the perturbation orders are chosen to obtain the higher-order corrections.

The leading-order terms satisfy exactly the boundary conditions at $r = R_{\text{in}}$,

$$\sigma_{rr}^{\text{in}} = T_{\text{in}}, \quad \sigma_{r\theta}^{\text{in}} = 0. \quad (5.5)$$

To obtain a non-trivial solution for the higher-order terms, we relax the boundary conditions and instead require that the resultant forces satisfy the null boundary conditions in an average sense:

$$\int_0^{2\pi} R_{\text{in}} \sigma_{rr}^{(1)} d\theta = \int_0^{2\pi} R_{\text{in}} \sigma_{r\theta}^{(1)} d\theta = 0, \quad \text{at } r = R_{\text{in}}. \quad (5.6)$$

From the equilibrium equations in polar coordinates, retaining terms up to $\mathcal{O}(\zeta^{-2})$, leads to

$$\frac{\partial \left(r \sigma_{rr}^{(1)} \right)}{\partial r} + \frac{\partial \sigma_{r\theta}^{(1)}}{\partial \theta} - \frac{\sigma_{\theta\theta}^{(1)}}{\zeta} = 0, \quad r \frac{\partial \sigma_{r\theta}^{(1)}}{\partial r} + \frac{\partial \sigma_{\theta\theta}^{(1)}}{\partial \theta} \frac{1}{\zeta} + 2\sigma_{r\theta}^{(1)} = 0. \quad (5.7)$$

It then follows from these equations that

$$\sigma_{r\theta}^{(1)} = \frac{C_1(\theta)}{r^2}, \quad \sigma_{rr}^{(1)} = \frac{C_1'(\theta)}{r^2} + \frac{C_2(\theta)}{r}, \quad (5.8)$$

where $C_1(\theta)$ and $C_2(\theta)$ are unknown functions. The auxiliary equation (5.2)₃ yields

$$\left(T_{\text{in}} \frac{R_{\text{in}}}{r} + \frac{1}{\zeta} \sigma_{rr}^{(1)}\right) \frac{1}{\zeta^2} \sigma_{\theta\theta}^{(1)} - \frac{1}{\zeta^2} \left(\sigma_{r\theta}^{(1)}\right)^2 = 0. \quad (5.9)$$

We solve the $\mathcal{O}(\zeta^{-2})$ equation of (5.9) to obtain

$$\sigma_{\theta\theta}^{(1)} = \frac{C_1^2(\theta)}{r^3 T_{\text{in}} R_{\text{in}}}. \quad (5.10)$$

Note that the continuity condition at $r = W_{\text{FT}}$ imposes

$$\mathbf{n} \cdot \boldsymbol{\sigma}^{\text{in}} \mathbf{n} = \mathbf{n} \cdot \boldsymbol{\sigma}^{\text{out}} \mathbf{n}, \quad \mathbf{t} \cdot \boldsymbol{\sigma}^{\text{in}} \mathbf{n} = \mathbf{t} \cdot \boldsymbol{\sigma}^{\text{out}} \mathbf{n}, \quad (5.11)$$

where the superscript ‘in’ (‘out’) indicates the stress tensor inside (outside) the wrinkled region and the normal and tangent vectors of the surface $W_{\text{FT}} = R_{\text{in}}\gamma/2 + W^{(1)}(\theta)/\zeta$ is given by

$$\mathbf{n} = -\mathbf{e}_r + 2(W^{(1)})' / (\zeta R_{\text{in}} \gamma) \mathbf{e}_\theta, \quad \mathbf{t} = \mathbf{e}_\theta + 2(W^{(1)})' / (\zeta R_{\text{in}} \gamma) \mathbf{e}_r. \quad (5.12)$$

Next, we consider the solutions in the flat region. Note that in the large-separation limit, the stresses recover their counterparts in the classic Lamé problem, as given in (B.5). Under this correspondence, we give the outer solution through replacing R_{in} by W_{FT} and T_{in} by $T(W_{\text{FT}})$ in (B.5). Accordingly, we obtain

$$\begin{aligned} \sigma_{rr}^{\text{out}} &= T_{\text{out}} + \frac{(T_{\text{in}} - T_{\text{out}})\gamma^2 R_{\text{in}}^2}{4r^2} + \left(\frac{\gamma^2 R_{\text{in}}^2 (T_{\text{in}} - T_{\text{out}}) (\cos \theta \gamma R_{\text{in}} - 2W^{(1)}(\theta))}{4r^3} \right) \frac{1}{\zeta} + \mathcal{O}(\zeta^{-2}), \\ \sigma_{r\theta}^{\text{out}} &= \frac{\gamma^3 R_{\text{in}}^3 (T_{\text{in}} - T_{\text{out}})}{4r^3 \zeta} \sin \theta + \mathcal{O}(\zeta^{-2}), \\ \sigma_{\theta\theta}^{\text{out}} &= T_{\text{out}} - \frac{(T_{\text{in}} - T_{\text{out}})\gamma^2 R_{\text{in}}^2}{4r^2} - \left(\frac{\gamma^2 R_{\text{in}}^2 (T_{\text{in}} - T_{\text{out}}) (\cos \theta \gamma R_{\text{in}} - 2W^{(1)}(\theta))}{4r^3} \right) \frac{1}{\zeta} + \mathcal{O}(\zeta^{-2}). \end{aligned} \quad (5.13)$$

Since the hoop stress $\sigma_{\theta\theta}$ is continuous across the boundary between the wrinkled and non-wrinkled regions (Davidovitch et al., 2011) we can substitute (5.4) and (5.13) into (5.11), to obtain

$$W^{(1)}(\theta) = \frac{\gamma \cos \theta}{4} R_{\text{in}}, \quad C_1(\theta) = \frac{R_{\text{in}}^2 T_{\text{in}}}{4} \gamma \sin \theta, \quad C_2 = 0. \quad (5.14)$$

It can be readily verified that the boundary conditions in (5.6) are satisfied. Finally, for the far-from-threshold regime, the extent of the wrinkled region is given by (a can be replaced by ζ using (B.2))

$$W_{\text{FT}} = \frac{\gamma}{2} R_{\text{in}} + \frac{\gamma \cos \theta}{4\zeta} R_{\text{in}} + \mathcal{O}(\zeta^{-2}). \quad (5.15)$$

Since the second term depends on θ , the longest wrinkles appear at $\theta = 0$ and π , corresponding to two points on the x -axis located at the rear sides of the holes.

6. Experimental validation

In this section, we present an experimental study of the wrinkling threshold — this is the experimentally observable quantity that we have been able to best understand. In our model problem, the thin sheet is loaded by gradually increasing the tension ratio γ beyond one. To induce circumferential wrinkling in thin PS films, a water droplet can be placed onto the film, leading to wrinkle formation due to the capillary force exerted by the surface tension at the air–water–PS contact line (Huang et al., 2007; Vella et al., 2010; Schroll et al., 2013). Similarly, wrinkling can also be induced by poking a thin film or shell (Vella et al., 2011; Box et al., 2017; Vella and Davidovitch, 2018; Box et al., 2019; Wang et al., 2023). However, in these loading scenarios, the stress state is fixed once a droplet is applied, making it difficult to continuously increase the stress exerted on the film. To overcome this limitation, we follow the experimental setup described in (Piñeirua et al., 2013; Paulsen et al., 2017) and use a controlled differential surface tension to impose γ . This is achieved by confining a sheet to a water–air interface and using a Langmuir trough (left panel of Figure 10) to control the concentration of surfactant outside the film (and hence the effective tension T_{out}). The interface within the holes remains pure throughout, and hence the tension T_{in} remains at the interfacial tension of water throughout.

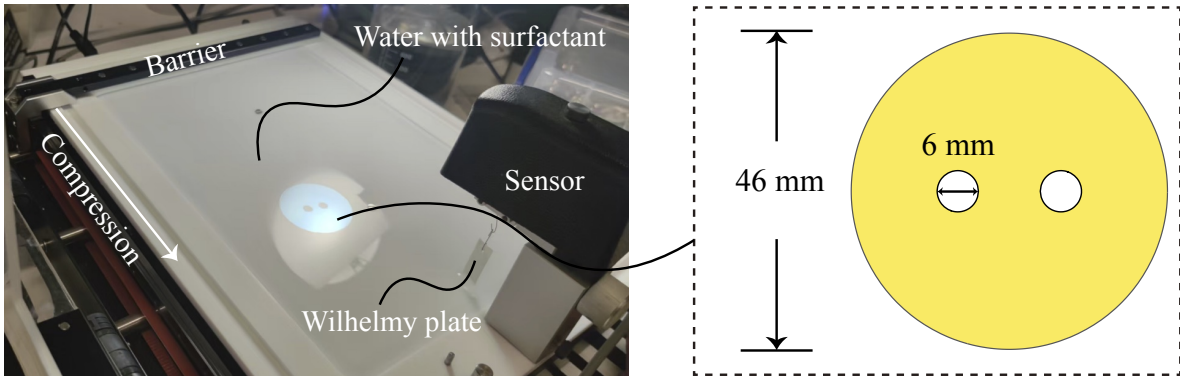


Figure 10: Illustration of the experimental setup. (Left) A Langmuir trough (NIMA 601) is used to load a thin film containing two circular holes by varying the concentration of surfactant at the interface outside the sheet. The interfacial tension of the external interface is measured using a Wilhelmy plate. (Right) Geometry of the sheet: The sheet has an overall circular shape with a diameter of 46 mm, while each of the two circular holes has a diameter of 6 mm.

We briefly introduce the materials and loading strategy used in our experiments. PS sheets (Young’s modulus 3.4 GPa, Poisson’s ratio 0.34, and thickness 166 nm) are fabricated on glass substrates by spin coating the dissolved PS powder (Goodfellow) in toluene (anhydrous, 99.8%; Sigma-Aldrich) and then cut into a circular shape with two circular holes, as shown in the right panel of Figure 10. To precisely control the geometric dimensions, we use a custom-designed template manufactured by laser cutting. Four cases are considered, corresponding to $\zeta = 0.5, 1, 1.5,$ and 3 . All samples have the same overall diameter of 46 mm and a hole diameter of 6 mm. The film is peeled off from the glass substrate using a deep water-filled beaker, after which it floats on the water surface. The floating film is then transferred into the Langmuir trough using a Petri dish.

At the beginning of each experiment, the trough contains deionized water, so that the PS film is subjected to uniform tensions $T_{\text{in}} \approx 72 \text{ mN/m}$ and $T_{\text{out}} \approx 72 \text{ mN/m}$, corresponding to the surface tension of clean water; $\gamma = 1$ initially. We then add the insoluble surfactant DPPC (dipalmitoylphosphatidylcholine) to the trough region outside the film by spreading from a chlorophorm

solution. As a result, the outer surface tension T_{out} decreases, and its value is measured using a Wilhelmy plate. Upon moving inwards the barrier in the trough, the available trough area is reduced and the DPPC concentration increases, thereby decreasing the tension T_{out} applied at the outer boundary. Yet the surface tension T_{in} within the two holes remains unchanged during barrier compression because DPPC is insoluble in the water subphase. Consequently, as the barrier is moved toward the film, the tension ratio γ increases and the film is loaded. Meanwhile, γ can be precisely regulated.

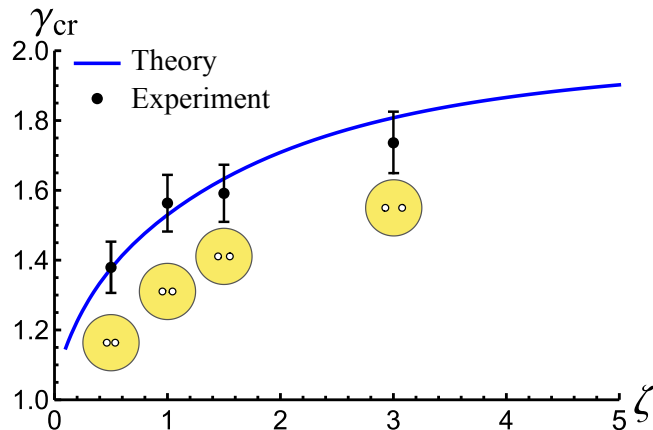


Figure 11: Comparison of the experimentally observed wrinkling threshold with the theoretical prediction. An error bar ($\pm 5\%$) and the geometry of the associated sample are indicated.

We perform each experiment in the Langmuir trough and record the deformation process using a camera (Canon EOS 6D). The outer tension T_{out} is documented at a rate of one measurement per second whilst the barrier speed is 3 cm/min. Guided by the near-threshold analysis in Section 5.1, we identify the onset of wrinkling around the hole and compare the experimental results with the theoretical prediction in Figure 11. The black dots correspond to the experimental data, while the solid curve represents the theoretical prediction with the sample geometry used in each experiment below the corresponding data point. Since tensional wrinkling is a supercritical bifurcation, it is not sensitive to imperfections. Additionally, the wrinkle amplitude grows gradually from zero. Taking this into account, we include a $\pm 5\%$ error bar. The experimental results agree well with our theoretical predictions. We therefore infer that, during the deformation process, the effects of sheet thickness, liquid density, Young’s modulus of the sheet, and gravity are negligible, as these factors do not enter the model for determining the threshold. These parameters, however, are known to affect the wrinkle number and amplitude (Coman and Bassom, 2007; Davidovitch et al., 2011; Schroll et al., 2013).

Finally, we present three snapshots of the wrinkled state in Figure 12 for tension ratios beyond the near-threshold regime. The distance ratio and the corresponding tension ratio are given in each panel. In all cases, the tension ratio remains below $2\gamma_{\text{in}}$, which might be expected to be close to the near-threshold regime. Nevertheless, wrinkles are observed to connect the two holes in all panels, even for $\zeta = 3$. In particular, the wrinkles are localized in the central region between the two holes as well as in the back region as predicted by our near-threshold analysis. For comparison, the boundary of the wrinkled region predicted by the near-threshold analysis is also highlighted by a blue dashed line. However, the actual extent of the wrinkled regions on the back sides is significantly larger than that predicted by the near-threshold theory. We note that, in both the Lamé problem and the annular geometry, wrinkles are uniformly distributed around the hole

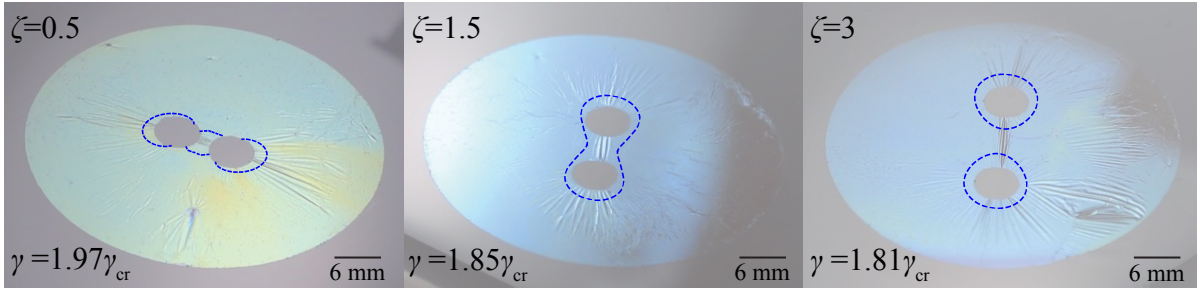


Figure 12: Snapshots of the wrinkled morphology as the tension ratio γ exceeds the near-threshold regime. The critical tension ratio γ_{cr} takes the values 1.3765, 1.6331, and 1.8079 in the left, middle, and right panels, respectively. For comparison, the boundary of the wrinkled region predicted by the near-threshold analysis is shown as a blue dashed line in each panel.

(Huang et al., 2007; Piñeirua et al., 2013; Paulsen et al., 2017; Box et al., 2019). In contrast, the presence of an additional hole breaks the radial symmetry, and the maximum wrinkle extent is observed along the direction connecting the centers of the two holes. This direction can therefore be identified as the preferred, or principal, direction of wrinkling. Furthermore, as discussed in Davidovitch et al. (2011), the wrinkle extent W_{FT} in the far-from-threshold regime of the Lamé problem reads $W_{\text{FT}} = \gamma R_{\text{in}}/2$. In the bipolar problem considered here, a rough estimate from Figure 12 shows that the maximum W_{FT} is much larger than $\gamma R_{\text{in}}/2$ ($\approx \gamma_{\text{cr}} R_{\text{in}}$ in all three cases), indicating that deformation or stress information can be transmitted over a longer distance and along a preferred direction.

7. Conclusions

We have studied the tension-induced wrinkling in thin elastic sheets containing two circular holes. We focussed on thin sheets that have negligible bending stiffness and cannot support compressive stresses. An analytical solution to the pre-buckled state was obtained using bipolar coordinates. As a result, we derived the critical tension ratio γ_{cr} beyond which wrinkling is expected to take place. We further performed asymptotic analysis of the case in which the two holes are well-separated, obtaining excellent approximations for γ_{cr} . Near-threshold wrinkling was analyzed in detail to primarily unravel the basic feature of wrinkling initiation and evolution. We find that wrinkles first occur at the area between the two holes and then gradually expands to the back sides. Further, we derived a perturbative solution for the far-from-threshold scenario and obtained qualitative information concerning the wrinkle distribution.

To test our predictions, we carried out experimental investigations using a Langmuir trough to generate wrinkling in a circular PS sheet that contains two circular holes. The predicted critical tension ratio γ_{cr} was validated. Experimental snapshots of the wrinkle morphology in the regime where the tension ratio γ exceeds the critical threshold are presented, providing novel insight into the wrinkle distribution. In comparison with the far-from-threshold results for the Lamé problem, we find that a much larger wrinkle extent is achieved experimentally. Specifically, the breaking of radial symmetry induces a preferred (or principal) direction along which the wrinkle extent attains its maximum reach. We expect that the results presented in this paper may also shed new light on wrinkling phenomena in thin films induced by multiple surface bubbles (Oratis et al., 2020). We also note that the wrinkles shown in Figure 12 with $\gamma \sim 2\gamma_{\text{in}}$ extend close to the outer circular edge of the sheet. When these wrinkles reach the edge, we would expect that other deformation modes become available to the sheet, including folding (Paulsen et al., 2017).

Tension-induced wrinkling in elastic films is not only of fundamental interest in thin-film mechanics but also has significant potential for evaluating forces generated by cell traction (Cerda and Mahadevan, 2003; Style et al., 2014; Li et al., 2022). Additionally, growing evidence show that mechanical cues can be sensed by cells to regulate their migration, differentiation, and collective cell behaviors (Engler et al., 2006; Ladoux and Mège, 2017; Vining and Mooney, 2017; Petridou et al., 2017; Murthy et al., 2017; Van Helvert et al., 2018). In this context, the Lamé problem provides an instructive analogy for understanding the situation in which a single cell contracts on a compliant substrate. A remarkable result is that the stress distribution can be regulated by wrinkling, such that the maximum stress decays inversely with distance rather than with its square, thereby enabling force transmission over longer ranges (Davidovitch et al., 2011). It is well known that cells can respond to long-range signals generated by other cells (Alisafaei et al., 2021). For the case of two cells, our model offers preliminary insights on the critical tension needed to generate wrinkles and their distributions.

Acknowledgment

This work was supported by a grant from the National Natural Science Foundation of China (Project No. 12372072). Y.L. and A.G. acknowledge the UKRI Horizon Europe Guarantee MSCA (Marie Skłodowska-Curie Actions) Postdoctoral Fellowship (EPSRC Grant No. EP/Y030559/1). S.R. acknowledges the Wolfson Visiting Fellowship, which provided support during her sabbatical visit to the University of Cambridge. We thank Dr. Aleksandra Ardaševa for helpful discussions at the early stages of this project, and Dr. Ben Fudge at University of Oxford for assisting the laser cutting. Y.L. also thanks Dr. Ming Dai at Nanjing University of Aeronautics and Astronautics for insightful discussions of stress divergence when two holes are extremely close.

Appendix A. Standard results for a bipolar coordinate system

In this Appendix, we briefly summarize some standard results expressed in bipolar coordinates.

Appendix A.1. Coordinate system

Let $\{\mathbf{e}_\tau, \mathbf{e}_\xi\}$ be the bipolar orthonormal basis while $\{\mathbf{e}_1, \mathbf{e}_2\}$ is the Cartesian one, then we have

$$\mathbf{e}_\tau = \frac{1 - \cos \xi \cosh \tau}{\cosh \tau - \cos \xi} \mathbf{e}_1 - \frac{\sin \xi \sinh \tau}{\cosh \tau - \cos \xi} \mathbf{e}_2, \quad \mathbf{e}_\xi = -\frac{\sin \xi \sinh \tau}{\cosh \tau - \cos \xi} \mathbf{e}_1 + \frac{\cos \xi \cosh \tau - 1}{\cosh \tau - \cos \xi} \mathbf{e}_2, \quad (\text{A.1})$$

and, conversely,

$$\mathbf{e}_1 = \frac{1 - \cos \xi \cosh \tau}{\cosh \tau - \cos \xi} \mathbf{e}_\tau + \frac{\sin \xi \sinh \tau}{\cosh \tau - \cos \xi} \mathbf{e}_\xi, \quad \mathbf{e}_2 = -\frac{\sin \xi \sinh \tau}{\cosh \tau - \cos \xi} \mathbf{e}_\tau + \frac{\cos \xi \cosh \tau - 1}{\cosh \tau - \cos \xi} \mathbf{e}_\xi. \quad (\text{A.2})$$

From (A.1), we obtain

$$\frac{\partial \mathbf{e}_\tau}{\partial \tau} = \frac{h \sin \xi}{a} \mathbf{e}_\xi, \quad \frac{\partial \mathbf{e}_\tau}{\partial \xi} = -\frac{h \sinh \tau}{a} \mathbf{e}_\xi, \quad \frac{\partial \mathbf{e}_\xi}{\partial \tau} = -\frac{h \sin \xi}{a} \mathbf{e}_\tau, \quad \frac{\partial \mathbf{e}_\xi}{\partial \xi} = \frac{h \sinh \tau}{a} \mathbf{e}_\tau. \quad (\text{A.3})$$

Appendix A.2. Stress tensor and equations of equilibrium

In the plane, we can write the Cauchy stress tensor with respect to the bipolar basis as

$$\boldsymbol{\sigma} = \sigma_{\tau\tau} \mathbf{e}_\tau \otimes \mathbf{e}_\tau + \sigma_{\tau\xi} \mathbf{e}_\tau \otimes \mathbf{e}_\xi + \sigma_{\tau\xi} \mathbf{e}_\xi \otimes \mathbf{e}_\tau + \sigma_{\xi\xi} \mathbf{e}_\xi \otimes \mathbf{e}_\xi. \quad (\text{A.4})$$

Using the definition of divergence operator in terms of a general orthonormal coordinate system (see p. 268 of Goriely, 2017, for example) and the scale factor (2.8), we arrive at

$$\begin{aligned} \frac{1}{h} \frac{\partial \sigma_{\tau\tau}}{\partial \tau} + \frac{1}{h} \frac{\partial \sigma_{\tau\xi}}{\partial \xi} + \frac{\sinh \tau}{a} (\sigma_{\xi\xi} - \sigma_{\tau\tau}) - \frac{2 \sin \xi}{a} \sigma_{\tau\xi} &= 0, \\ \frac{1}{h} \frac{\partial \sigma_{\xi\xi}}{\partial \xi} + \frac{1}{h} \frac{\partial \sigma_{\tau\xi}}{\partial \tau} + \frac{\sin \xi}{a} (\sigma_{\tau\tau} - \sigma_{\xi\xi}) - \frac{2 \sinh \tau}{a} \sigma_{\tau\xi} &= 0. \end{aligned} \quad (\text{A.5})$$

The strain components ε_{ij} in bipolar coordinates are:

$$\begin{aligned} \varepsilon_{\tau\tau} &= \frac{1}{h} \frac{\partial u}{\partial \tau} - \frac{v \sin \xi}{a}, & \varepsilon_{\xi\xi} &= \frac{1}{h} \frac{\partial v}{\partial \xi} - \frac{u \sinh \tau}{a}, \\ \varepsilon_{\tau\xi} &= \frac{1}{2} \left(\frac{1}{h} \frac{\partial v}{\partial \tau} + \frac{1}{h} \frac{\partial u}{\partial \xi} + \frac{u \sin \xi}{a} + \frac{v \sinh \tau}{a} \right), \end{aligned} \quad (\text{A.6})$$

where $u(\tau, \xi)$ and $v(\tau, \xi)$ are displacement components in ξ - and τ -directions, respectively.

Appendix A.3. Airy stress function

In the bipolar geometry used here the stress components are given in terms of ψ by (Jeffery, 1921; Ling, 1948; Wu and Nowinski, 1970; Lucht, 2015)

$$\sigma_{\tau\tau} = \frac{1}{a} \left((\cosh \tau - \cos \xi) \frac{\partial^2}{\partial \xi^2} - \sinh \tau \frac{\partial}{\partial \tau} - \sin \xi \frac{\partial}{\partial \xi} + \cosh \tau \right) \frac{\psi}{h}, \quad (\text{A.7})$$

$$\sigma_{\xi\xi} = \frac{1}{a} \left((\cosh \tau - \cos \xi) \frac{\partial^2}{\partial \tau^2} - \sinh \tau \frac{\partial}{\partial \tau} - \sin \xi \frac{\partial}{\partial \xi} + \cos \xi \right) \frac{\psi}{h}, \quad (\text{A.8})$$

$$\sigma_{\tau\xi} = -\frac{1}{a} (\cosh \tau - \cos \xi) \frac{\partial^2 \psi}{\partial \tau \partial \xi}. \quad (\text{A.9})$$

Appendix B. Derivation of the approximate stresses in the far-distance limit of two holes

In this Appendix, we derive the asymptotic expressions for the stress components in the limit $\zeta \rightarrow \infty$. Referring to Figure 2, we identify

$$\xi = \theta_1 - \theta_2, \quad d_1^2 = r_1^2 + r_2^2 - 2r_1 r_2 \cos \xi, \quad (\text{B.1})$$

where the second relation follows directly from the law of cosines. Moreover, from (2.6)₁ and (4.3), we obtain

$$a = R_{\text{in}} \sinh \tau_{\text{in}} = \frac{\sqrt{\zeta(\zeta + 4)}}{2} R_{\text{in}}. \quad (\text{B.2})$$

To proceed further, we introduce the following scaling for large ζ :

$$r_1 \sim \frac{a}{\sinh \tau}, \quad (\text{B.3})$$

where τ denotes the bipolar coordinate of the material point shown in Figure 2.

It is expected that as $\zeta \rightarrow \infty$, $\sigma_{\tau\tau}$ will reduce to the σ_{rr} (the polar coordinates are used for the classic Lamé problem). Furthermore, we make use of the identities

$$\begin{aligned} r_2^2 &= r_1^2 + d_1^2 + 2r_1d_1 \cos \theta_1, & \cos \xi &= \frac{r_1 + d_1 \cos \theta_1}{r_2}, \\ \sin \xi &= \frac{d_1 \sin \theta_1}{r_2}, & \cos 2\xi &= \frac{r_1^2 + 2r_1d_1 \cos \theta_1 + d_1^2 \cos 2\theta_1}{r_2^2}, \end{aligned} \quad (\text{B.4})$$

and then take the series expansions of (3.14)-(3.16) to obtain

$$\begin{aligned} \sigma_{\tau\tau} &= T_{\text{out}} + (T_{\text{in}} - T_{\text{out}}) \frac{R_{\text{in}}^2}{r_1^2} + \frac{2(T_{\text{in}} - T_{\text{out}}) \cos \theta_1}{\zeta} \frac{R_{\text{in}}^3}{r_1^3} + \mathcal{O}(\zeta^{-2}), \\ \sigma_{\tau\xi} &= 2(T_{\text{in}} - T_{\text{out}}) \frac{R_{\text{in}}(r_1^2 - R_{\text{in}}^2)}{r_1^3 \zeta} \sin \theta_1 + \mathcal{O}(\zeta^{-2}), \\ \sigma_{\xi\xi} &= T_{\text{out}} - (T_{\text{in}} - T_{\text{out}}) \frac{R_{\text{in}}^2}{r_1^2} - \frac{2(T_{\text{in}} - T_{\text{out}}) \cos \theta_1}{\zeta} \frac{R_{\text{in}}^3}{r_1^3} + \mathcal{O}(\zeta^{-2}). \end{aligned} \quad (\text{B.5})$$

It can be seen that, as $\zeta \rightarrow \infty$, stresses in (B.5) fully recover the classical Lamé solution (Timoshenko and Goodier, 1951; Coman and Bassom, 2007; Davidovitch et al., 2011). We point out that the terms of $\mathcal{O}(\zeta^{-2})$ are lengthy so we omit them here.

According to (B.5) with terms of $O(\zeta^{-2})$ being involved, we can also determine the threshold γ_{cr} . To this end, we write down the coordinate r_1 at the inner boundary, and it is actually related to R_{in} by

$$r_1^2 + a^2 (\coth \tau_{\text{in}} - 1)^2 - 2r_1a (\coth \tau_{\text{in}} - 1) \cos \theta_1 = R_{\text{in}}^2. \quad (\text{B.6})$$

Combining the fact that $R_{\text{in}} = a/\sinh \tau_{\text{in}}$ and $\tau_{\text{in}} = \text{arccosh}(\zeta/2 + 1)$, we denote the coordinate at the inner boundary in terms of θ_1 and ζ . Finally, from the equation $\sigma_2 = 0$ we derive

$$\gamma = 2 - \frac{4 \cos 2\theta_1}{\zeta^2} + \frac{2(2 \cos \theta_1 + 8 \cos 2\theta_1 + 2 \cos 3\theta_1)}{\zeta^3} + \mathcal{O}(\zeta^{-4}), \quad (\text{B.7})$$

which attains a minimum at $\theta_1 = \pi$ with the associated critical tension ratio given by

$$\gamma_{\text{cr}} = 2 - \frac{4}{\zeta^2} + \frac{8}{\zeta^3} + \mathcal{O}(\zeta^{-3}), \quad (\text{B.8})$$

which is consistent with (4.7) up to $\mathcal{O}(\zeta^{-3})$. This validates the consistency of our asymptotic analysis.

References

Alisafaei, F., Chen, X., Leahy, T., Janmey, P.A., Shenoy, V.B., 2021. Long-range mechanical signaling in biological systems. *Soft Matter* 17, 241–253.

- Andrade-Silva, I., Adda-Bedia, M., 2019. Pre-buckled states of a stretched sheet with an elliptic hole. *Europhysics Letters* 128, 14004.
- Ardaševa, A., Venkatesh, V., Matsunaga, D., Deguchi, S., Doostmohammadi, A., 2026. Cell-induced wrinkling patterns on soft substrates. *arxiv* , 2603.12839.
- Baker, G.A., Graves-Morris, P., 1996. Padé Approximants. *Encyclopedia of Mathematics and its Applications*. 2 ed., Cambridge University Press.
- Bowden, N., Brittain, S., Evans, A.G., Hutchinson, J.W., Whitesides, G.M., 1998. Spontaneous formation of ordered structures in thin films of metals supported on an elastomeric polymer. *nature* 393, 146–149.
- Box, F., Domino, L., Corvo, T.O., Adda-Bedia, M., Démery, V., Vella, D., Davidovitch, B., 2023. Delamination from an adhesive sphere: Curvature-induced dewetting versus buckling. *Proceedings of the National Academy of Sciences* 120, e2212290120.
- Box, F., O’Kiely, D., Kodio, O., Inizan, M., Castrejón-Pita, A.A., Vella, D., 2019. Dynamics of wrinkling in ultrathin elastic sheets. *Proceedings of the National Academy of Sciences* 116, 20875–20880.
- Box, F., Vella, D., Style, R.W., Neufeld, J.A., 2017. Indentation of a floating elastic sheet: geometry versus applied tension. *Proceedings of the Royal Society A: Mathematical, Physical and Engineering Sciences* 473, 20170335.
- Callias, C.J., Markenscoff, X., 1989. Singular asymptotics analysis for the singularity at a hole near a boundary. *Quarterly of applied mathematics* 47, 233–245.
- Callias, C.J., Markenscoff, X., 1993. The singularity of the stress field of two nearby holes in a planar elastic medium. *Quarterly of applied mathematics* 51, 547–557.
- Cerda, E., Mahadevan, L., 2003. Geometry and physics of wrinkling. *Physical Review Letters* 90, 074302.
- Chai, P.P., Liu, Y., Wang, F.F., 2024. Stretch-induced wrinkling of anisotropic hyperelastic thin films. *Thin-Walled Structures* 200, 111961.
- Coman, C., Haughton, D., 2006. Localized wrinkling instabilities in radially stretched annular thin films. *Acta Mechanica* 185, 179–200.
- Coman, C.D., Bassom, A.P., 2007. On the wrinkling of a pre-stressed annular thin film in tension. *Journal of the Mechanics and Physics of Solids* 55, 1601–1617.
- Dai, Z., Lu, N., 2021. Poking and bulging of suspended thin sheets: Slippage, instabilities, and metrology. *Journal of the Mechanics and Physics of Solids* 149, 104320.
- Davidovitch, B., Klein, A., 2024. How viscous bubbles collapse: Topological and symmetry-breaking instabilities in curvature-driven hydrodynamics. *Proc. Natl Acad. Sci.* 121, e2310195121.

- Davidovitch, B., Schroll, R.D., Vella, D., Adda-Bedia, M., Cerda, E.A., 2011. Prototypical model for tensional wrinkling in thin sheets. *Proceedings of the National Academy of Sciences* 108, 18227–18232.
- Engler, A.J., Sen, S., Sweeney, H.L., Discher, D.E., 2006. Matrix elasticity directs stem cell lineage specification. *Cell* 126, 677–689.
- Goriely, A., 2017. The mathematics and mechanics of biological growth. volume 45 of *Interdisciplinary applied mathematics*. 1 ed., Springer-Verlag, New York. doi:10.1007/978-0-387-87710-5.
- Hohlfeld, E., Davidovitch, B., 2015. Sheet on a deformable sphere: Wrinkle patterns suppress curvature-induced delamination. *Physical Review E* 91, 012407.
- Huang, J., 2010. Wrinkling of Floating Thin Polymer Films. Ph.D. thesis. University of Massachusetts - Amherst.
- Huang, J., Juskiewicz, M., De Jeu, W.H., Cerda, E., Emrick, T., Menon, N., Russell, T.P., 2007. Capillary wrinkling of floating thin polymer films. *Science* 317, 650–653.
- Hure, J., Roman, B., Bico, J., 2012. Stamping and wrinkling of elastic plates. *Physical Review Letters* 109, 054302.
- Jeffery, G.B., 1921. IX. plane stress and plane strain in bipolar co-ordinates. *Philosophical Transactions of the Royal Society of London. Series A, Containing Papers of a Mathematical or Physical Character* 221, 265–293.
- Ladoux, B., Mège, R.M., 2017. Mechanobiology of collective cell behaviours. *Nature Reviews Molecular Cell Biology* 18, 743–757.
- Li, H., Matsunaga, D., Matsui, T.S., Aosaki, H., Kinoshita, G., Inoue, K., Doostmohammadi, A., Deguchi, S., 2022. Wrinkle force microscopy: a machine learning based approach to predict cell mechanics from images. *Communications Biology* 5, 361.
- Ling, C.B., 1948. On the stresses in a plate containing two circular holes. *Journal of Applied Physics* 19, 77–82.
- Liu, Y., Liu, R.C., Ma, W., Goriely, A., 2025. Post-buckling of fiber-reinforced soft tissues. *Journal of the Mechanics and Physics of Solids* 203, 106220.
- Liu, Z., Liu, Y., 2026. A brief review on recent progress of surface onstabilities in film–substrate systems. *Acta Mechanica Solida Sinica* 39, 433–454.
- Lucht, P., 2015. Bipolar coordinates and the two-cylinder capacitor. Rimrock Digital Technology, Salt Lake City, Utah 84103, 61.
- Mansfield, E.H., 1969. Tension field theory, a new approach which shows its duality with inextensional theory, in: *Applied Mechanics: Proceedings of the Twelfth International Congress of Applied Mechanics*, Stanford University, August 26–31, 1968, Springer. pp. 305–320.

- Murthy, S.E., Dubin, A.E., Patapoutian, A., 2017. Piezos thrive under pressure: mechanically activated ion channels in health and disease. *Nature Reviews Molecular Cell Biology* 18, 771–783.
- Oratis, A.T., Bush, J.W., Stone, H.A., Bird, J.C., 2020. A new wrinkle on liquid sheets: Turning the mechanism of viscous bubble collapse upside down. *Science* 369, 685–688.
- Paulsen, J.D., Démery, V., Toga, K.B., Qiu, Z., Russell, T.P., Davidovitch, B., Menon, N., 2017. Geometry-driven folding of a floating annular sheet. *Physical Review Letters* 118, 048004.
- Petridou, N.I., Spiró, Z., Heisenberg, C.P., 2017. Multiscale force sensing in development. *Nature Cell Biology* 19, 581–588.
- Piñeirua, M., Tanaka, N., Roman, B., Bico, J., 2013. Capillary buckling of a floating annulus. *Soft Matter* 9, 10985–10992.
- Pipkin, A.C., 1986. The relaxed energy density for isotropic elastic membranes. *IMA journal of applied mathematics* 36, 85–99.
- Pocivavsek, L., Dellsy, R., Kern, A., Johnson, S., Lin, B., Lee, K.Y.C., Cerda, E., 2008. Stress and fold localization in thin elastic membranes. *Science* 320, 912–916.
- Schroll, R., Adda-Bedia, M., Cerda, E., Huang, J., Menon, N., Russell, T., Toga, K., Vella, D., Davidovitch, B., 2013. Capillary deformations of bendable films. *Physical Review Letters* 111, 014301.
- Steigmann, D., Pipkin, A., 1989a. Finite deformations of wrinkled membranes. *The Quarterly Journal of Mechanics and Applied Mathematics* 42, 427–440.
- Steigmann, D.J., 1990. Tension-field theory. *Proceedings of the Royal Society of London. A. Mathematical and Physical Sciences* 429, 141–173.
- Steigmann, D.J., Pipkin, A.C., 1989b. Wrinkling of pressurized membranes. *Journal of Applied Mechanics* 56, 624–628.
- Style, R.W., Boltianskiy, R., German, G.K., Hyland, C., MacMinn, C.W., Mertz, A.F., Wilen, L.A., Xu, Y., Dufresne, E.R., 2014. Traction force microscopy in physics and biology. *Soft Matter* 10, 4047–4055.
- Timoshenko, S., Goodier, J.N., 1951. *Theory of Elasticity*. McGraw-Hill Book Company.
- Van Helvert, S., Storm, C., Friedl, P., 2018. Mechanoreciprocity in cell migration. *Nature Cell Biology* 20, 8–20.
- Vella, D., Adda-Bedia, M., Cerda, E., 2010. Capillary wrinkling of elastic membranes. *Soft Matter* 6, 5778–5782.
- Vella, D., Ajdari, A., Vaziri, A., Boudaoud, A., 2011. Wrinkling of pressurized elastic shells. *Physical Review Letters* 107, 174301.
- Vella, D., Davidovitch, B., 2018. Regimes of wrinkling in an indented floating elastic sheet. *Physical Review E* 98, 013003.

- Vella, D., Huang, J., Menon, N., Russell, T.P., Davidovitch, B., 2015. Indentation of ultrathin elastic films and the emergence of asymptotic isometry. *Physical Review Letters* 114, 014301.
- Vining, K.H., Mooney, D.J., 2017. Mechanical forces direct stem cell behaviour in development and regeneration. *Nature Reviews Molecular Cell Biology* 18, 728–742.
- Wang, T., Yang, Y., Xu, F., 2022. Mechanics of tension-induced film wrinkling and restabilization: a review. *Proceedings of the Royal Society A* 478, 20220149.
- Wang, W., Sun, Y., He, L., Ni, Y., 2023. Effects of viscosity and loading rate on wrinkling dynamics and coarsening of floating sheets. *International Journal of Solids and Structures* 281, 112434.
- Wu, L., Markenscoff, X., 1996. Singular stress amplification between two holes in tension. *Journal of elasticity* 44, 131–144.
- Wu, T., Nowinski, J., 1970. A general solution in bipolar coordinates to problems involving elastic dislocations. *SIAM Journal on Applied Mathematics* 19, 1–19.
- Zimmerman, R.W., 1988. Stress singularity around two nearby holes. *Mechanics Research Communications* 15, 87–90.